Topology and control design of a sinusoidal very low frequency high voltage generator

Zhigang LIU,* Guofeng LI, Ninghui WANG
Institute of Electrostatics and Special Power, Dalian University of Technology, Dalian, China

Abstract: To reduce the volume and the structural complexity of a very low frequency (VLF) high voltage (HV) generator, this paper introduces a novel sinusoidal VLF HV generator with 2 high frequency HV (HFHV) transformers and 2 metal-oxide semiconductor field-effect transistor cascaded HV bridge arms. Series-parallel resonant converter technology is applied to reduce the impact of the distributed parameters, decreasing the power loss and the volume of the transformer. Both the switching frequency and the duty cycle are utilized as actuating variables to cope with the large ranges of output. Simultaneously, the principle of segmental data processing is proposed to obtain different steady-state operating points, greatly reducing the calculation of the microcontroller unit (MCU), improving the accuracy of the control strategy, and the system response time. As a result, the control strategy is successfully achieved by the MCU dsPIC33FJ128MC706. The test of the 35 kV/0.1 Hz VLF HV power supply is taken on a capacitor (1.5 μF), which is equivalent to the cross-linked polyethylene cable in the electrical characteristics. When the input voltage varies between 180 V and 250 V, the accuracy of the sinusoidal VLF HV is 2%. The step change response time is less than 120 μs when the output changes from no-load to full-load. The total harmonic distortion is less than 1%, which meets the IEEE400.2 standard well. The total weight of the generator is less than 20 kg. The results of the experiment verify the accuracy and feasibility of the control theory and the topology.

Key words: Sinusoidal VLF high voltage, LCC resonant converter, segmental data processing

1. Introduction

Cross-linked polyethylene (XLPE) cable is extensively applied in the transmission and distribution of high voltage (HV) and ultra-HV power system for its excellent electrical performance, convenient paving, good antiaging feature, and extraordinary heat-resisting performance. With the mass production of XLPE cable, the requirement for the HV testing system is increasing. Compared with the direct current (DC) HV test system, the very low frequency (VLF) HV test system that was proposed in [1–3] does not accumulate charge in the insulation layer or damage the insulation of the cable. Considering the advantages in the volume, weight, and energy consumption of VLF HV test systems over power frequency HV test equipment, the VLF testing concept was adopted as a standard by the European Union in 1996 and by the International Electrotechnical Commission (IEC) in 2006 (IEC60060–3-2006). Hence, VLF HV power supply is the future tendency of the development of the XLPE cable HV test system.

In the early research efforts [4,5], the output voltage waveform of the VLF HV power supply was mainly nominal cosine-rectangular rather than sinusoidal waveform. Although it can be used in a XLPE cable test, the

*Correspondence: lvystdy@163.com

cosine-rectangular waveform is significantly different than the actual working conditions. Moreover, the cosine-rectangular waveform may easily cause a voltage overshoot, damaging the insulation of the cable. Although VLF sinusoidal waveform was obtained in [6,7], the volume and weight were still too large. The topology proposed in this paper adopts light high frequency HV (HFHV) transformers to replace the heavy power frequency transformer and autotransformer. Furthermore, closed-loop control technology is adopted in this paper, not only extending the input voltage range, but also improving the sinusoidal VLF HV output accuracy. The fault can be diagnosed quickly and accurately using this technology. Although the total harmonic distortion (THD) in [8] decreased to 2.32%, the output voltage level was low. To generate a higher voltage, more cascaded transformers were needed, making the control and structure complex. If some errors occur, solving the problems will be very time-consuming. The topology that is proposed in this paper has a simple structure, adopting a structural module design idea. Hence, problems can be quickly found and fixed. In [9], the VLF sinusoidal waveform was obtained through a single HFHV transformer. However, the full-bridge inverter determines that the secondary side cannot be grounded. As the voltage level rises, the HV sampling will be very difficult. Hence, we adopt 2 transformers to generate a positive and negative voltage relative to the ground, which ensures that the secondary HV will be directly sampled by the resistor divider. This method not only improves the safety of the circuit, but also reduces manufacturing costs. The low distortion sinusoidal VLF HV sinusoidal was obtained in [10], but the waveform was obtained by controlling the switches parallel to the resistor. The higher accuracy requires more switches and the control system introduced in [10] needed to turn each of the switches on and off over time. Hence, it is complex compared to the method of applying the metal-oxide semiconductor field-effect transistor (MOSFET) cascade technology that is adopted in this paper.

Although the HFHV transformer can reduce the size and weight of the equipment, the distributed parameter of the HFHV transformer cannot be ignored due to its high turn ratio and multilayer structure. Inevitably, the leakage inductance and the stray capacitance studied by [11,12] may induce an adverse impact on the system. Therefore, the system selects series-parallel resonant converter (LCC) technology according to the research results [13–15], which takes full advantage of the distributed parameter of the HFHV transformer. In this paper, the leakage inductance can serve as the series inductor of the LCC (1 in Figure 1), while the stray capacitance of the transformer can serve as the parallel capacitor of the LCC (2 in Figure 1), according to the research efforts in [16,17]. Both the converter switching frequency and the duty cycle are utilized as actuating variables to cope with the large ranges of output within a small range of switching frequency, which is different from the single frequency modulation or duty cycle modulation mentioned in [18]. By this method, a zero current switch (ZCS) is achieved; furthermore the HV rectifier diode can shut down naturally, improving the efficiency of the transformer and reducing the volume of the transformer. The structure of this paper is organized as follows: Section 2 provides the topology of the power supply. Section 3 is the theoretical analysis of the circuit according to the characteristics of the topology. The control strategy and the method of segmental data processing are discussed in Section 4. The experimental validation results are provided in Section 5. The final conclusions are given in Section 6.

2. Topology design

As illustrated in Figure 1, The VLF HV generator operating principle can be divided into 3 parts: boost part, high frequency part, and low frequency part (the black circle is the sampling point). The power frequency alternating current (AC) voltage is rectified and then boosted to a fixed DC voltage by the boost part. The function of the boost part is to stabilize the DC voltage; hence, the DC voltage can be treated as a constant,
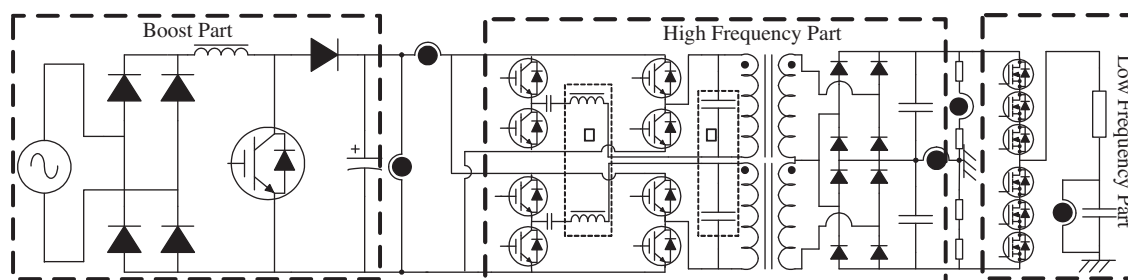
Figure 1. Topology of the sinusoidal VLF HV generator.

simplifying the design of the transformer and control strategy. Through the inverter, the HFHV step-up transformer, and the HV rectifier diode, the positive and negative DC HV can be obtained. After that, the capacitive load can be charged and discharged by the 2 HV bridge arms under the sinusoidal pulse width modulation control method. As the resistor and the capacitive load can be considered as a low-pass filter, the sinusoidal VLF HV is generated across the capacitive load. There are 3 key points about the design of the sinusoidal VLF HV generator. The first key point is that even if the VLF signal is modulated by a high frequency signal, the fundamental very low-frequency wave still cannot transform through the transformer as the restriction of the core materials and the series capacitor. Therefore, it needs to be rectified and inverted again on the secondary side of the transformer. The second key point is that the voltage across the output capacitor requires a bipolar sinusoidal waveform. The full-bridge inverter circuit with a single transformer cannot meet the requirements. Hence, this paper adopts 2 transformers to generate a positive and negative voltage, charging and discharging the capacitive load by applying the half-bridge inverter. The last key point is the HV bridge. Since many MOSFETs are in a series, one of the most important points is the equalization of the voltage difference due to each MOSFET's transient and static characteristics. Another important thing is the elimination of the turn on/off delay in the gate drive circuitry. Hence, the key points of designing the HV bridge up to several dozens of kilovolts or connecting the several dozens of MOSFETs are as follows:

- Select a MOSFET that has a short switching delay time, low input capacitance, and low output capacitance.

- Reduce the response time differences of each of the gate drives.

- Provide bias power voltage, which has several dozens of kilovolts isolation withstanding.

- Equal the voltage of each MOSFET.

According to the analysis and research efforts in [19–21], combining the load current and operating frequency of the low-frequency power (LFP), this paper presents the schematic of the HV bridge. As shown in Figure 2, the switch component is a MOSFET IXTF03N400, with an electrical isolation of 4 kV. D1 to D7 are the transient voltage suppressors (TVSs) P6KE500A, which are responsible for grading the voltage of the MOSFET IXTF03N400. Utilizing the internal freewheel diode of the MOSFET 2SK1413 (G1–G4) and the resistance-capacitance (RC) absorption circuit (Sn1 in Figure 2), the voltage spike can be inhibited effectively. Sn2 is the conventional RC-diode (RCD) clamp circuit. The schematic of the gate drive is illustrated in Figure 3. D8, D9, D11, and D12 are ultra-fast recovery diodes US1A. These diodes not only play the role of a rectifier, but also avoid the circulation of the current that is generated by the difference of the voltage between the positive and negative gates. D10 is the TVS diode P6KE15A, C_1 and C_2 are the accelerating capacitances,

which can decrease the rise and fall times of the MOSFET IXTF03N400. To reduce the leakage inductances of transformer, the core is made up of an amorphous alloy to minimize the number of winding turns, the shield lay between the primary and secondary is necessary to reduce the harmonics.
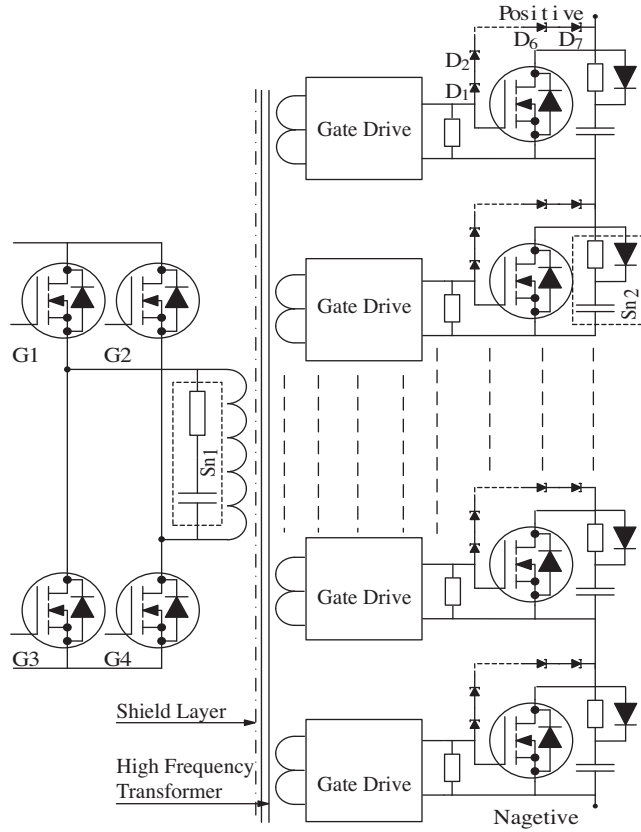

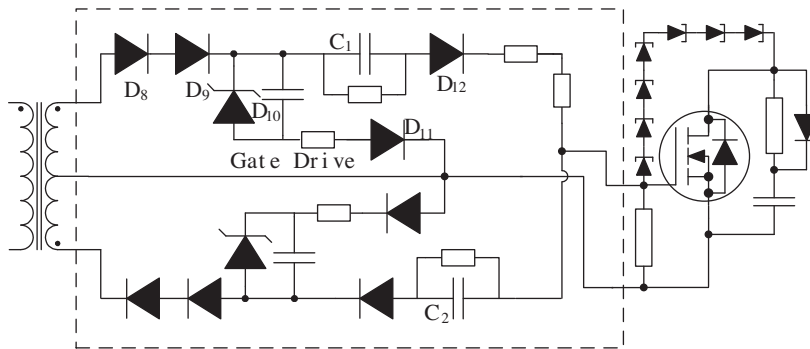
Figure 2. Schematic of a HV bridge arm.

Figure 3. Schematic of a simple gate drive system.

The main advantages of this topology are as follows:

- Light weight, small volume, and high efficiency.

- The secondary side has a grounded point. The system can sample the secondary voltage and current directly. Hence, the closed-loop control method can be achieved.

- The boost technology is applied in this paper, which is responsible for the prestabilizing of the voltage for the high frequency power (HFP). Hence, large-scale voltage operating is accomplished.

- The LCC resonant converter utilizes the distributed parameter of the HFHV transformer as parallel capacitance and series inductance sufficiently. As a result, the influence of the distributed parameter is decreased efficiently, the efficiency of the transformer is improved, and the volume of the transformer is also reduced.

3. Theoretical analysis

Note that the boost part is not analyzed in this paper due to its mature technology, and the turn ratio is defined as 1 to simplify the analysis. According to the different frequencies of different parts, the analysis of the operating principle is established in 2 parts. One is HFP and the other is LFP. A simplified circuit can be described by Figure 4 due to the symmetry.
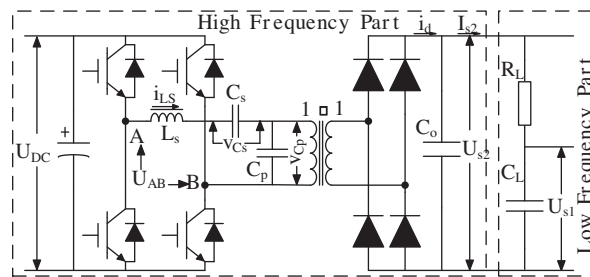

Figure 4. Simple circuit of the HFP and LFP.

For the HFP, it is complicated to analyze the circuit due to the multiple resonant components and complex resonant process. To simplify the analysis, $i_{Ls}(t), v_s(t), v_p(t)$, and $v_{AB}(t)$ can be approximated by the extended describing function and fundamental approximation method [22–24], according to the key waveform of the HFP shown in Figure 5.
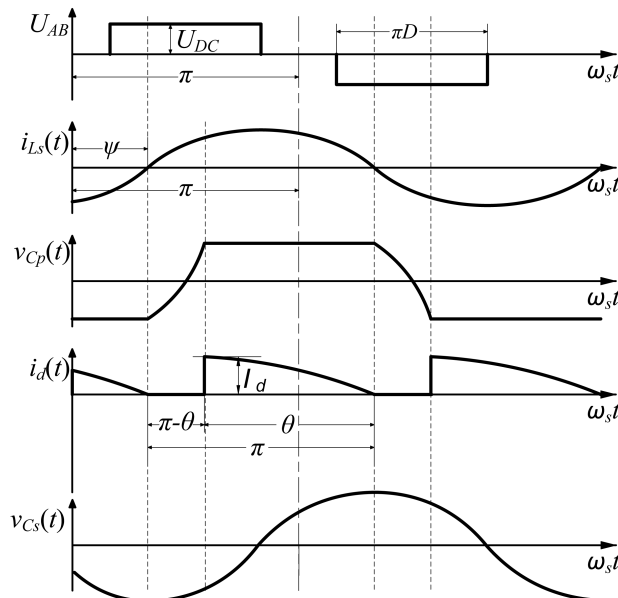

Figure 5. Key waveforms of the high frequency part.

$$i_{Ls}(t) = i_{Lss}(t)\sin(\omega_s t) + i_{Lsc}(t)\cos(\omega_s t),$$ (1a)

$$v_s(t) = v_{ss}(t)\sin(\omega_s t) + v_{sc}(t)\cos(\omega_s t),$$ (1b)

$$v_p(t) = v_{ps}(t)\sin(\omega_s t) + v_{pc}(t)\cos(\omega_s t),$$ (1c)

$$v_{AB}(t) = \frac{4V_{DC}}{\pi}\sin\left(\frac{D}{2}\pi\right)\sin\omega_s t.$$ (1d)

in which

$$v_{ps} = \frac{i_{Lsc}(\pi - \theta + \sin\theta\cos\theta) + i_{Lss}\sin^2\theta}{\pi\omega_s C_p},$$

$$v_{pc} = \frac{i_{Lsc}\sin^2\theta - i_{Lss}(\pi - \theta + \sin\theta\cos\theta)}{\pi C_p\omega_s},$$

$$i_{Ls} = \sqrt{i_{Lss}^2 + i_{Lsc}^2},$$

$$\theta = \arccos\left(\frac{2\omega_s C_p U_{s2}}{I_{Ls}} - 1\right).$$

According to Figure 4, the differential equation can be written as Eq. (2):

$$L_s\left(\frac{di_{Ls}(t)}{dt}\right) = v_{AB}(t) - v_{ss}(t) - v_{ps}(t),$$ (2a)

$$C_s\frac{dv_s(t)}{dt} = i_{Ls}(t),$$ (2b)

$$C_o\frac{dv_{s2}(t)}{dt} = i_{s2}(t) - \frac{v_{s2}(t)}{R_e}.$$ (2c)

According to Eq. (1), Eq. (2) can be rewritten by Eq. (3)

$$L_s\left(\frac{di_{Lss}}{dt}\right) = \frac{4}{\pi}V_{DC}\sin\left(\frac{d}{2}\pi\right) - v_{ss} - i_{Lss}\frac{\sin^2\theta}{\pi\omega_s C_p} + i_{Lsc}\frac{\pi\omega_s^2 L_s C_p - \pi + \theta + \sin\theta\cos\theta}{\pi\omega_s C_p},$$ (3a)

$$L_s\left(\frac{di_{Lsc}}{dt}\right) = L_s\omega_s i_{Lss} - v_{sc} - i_{Lsc}\frac{\sin^2\theta}{\pi\omega_s C_p} + i_{Lss}\frac{(\pi - \theta + \sin\theta\cos\theta)}{\pi\omega_s C_p},$$ (3b)

$$C_s\frac{dv_{ss}}{dt} = i_{Lss} + C_s\omega_s v_{sc},$$ (3c)

$$C_s\frac{dv_{sc}}{dt} = i_{Lsc} - C_s\omega_s v_{ss},$$ (3d)

$$C_o\frac{dv_{s2}}{dt} = \frac{\sqrt{i_{Lss}^2 + i_{Lsc}^2}}{\pi}(1 - \cos\theta) + \frac{v_{s2}}{R_e}.$$ (3e)

Eqs. (3a)–(3e) are a nonlinear large-signal model about i_{Lss}, i_{Lsc}, v_{ss}, v_{sc}, v_{s2}. In order to find the small-signal model for the series-parallel resonant converter with a capacitive output filter, the first step is to obtain a steady-state operating point for the system. The steady-state operation point can be described by Eq. (4):

$$M = \frac{V_{s2}}{V_{in}} = \frac{4}{\pi} \cdot \frac{k_{21}}{k_v} \cdot \sin(D \cdot \frac{\pi}{2}) \cdot n, \tag{4a}$$

$$k_v = 1 + 0.27 \cdot \sin\left(\frac{\theta}{2}\right), \tag{4b}$$

$$\theta = 4 \arctan\sqrt{\frac{2 \cdot \pi \cdot Q \cdot n^2}{f_{sN} \cdot \alpha}} \quad Q = \frac{\sqrt{L_s/C_s}}{R_e}, \tag{4c}$$

$$f_{sN} = \frac{f_s}{f_0} \quad f_0 = \frac{1}{2\pi\sqrt{L_sC_s}}, \tag{4d}$$

$$k_{21} = \frac{v_{cp(1)}}{v_{AB(1)}} = \frac{1}{\sqrt{[1 - \alpha(f_{sN} - 1)(1 + \frac{\tan(|\beta|)}{wC_pR_e})]^2 + [\alpha(f_{sN}^2 - 1) \cdot \frac{1}{wC_pR_e}]^2}}, \tag{4e}$$

$$\beta = -0.4363 \cdot \sin(\theta)wC_pR_e = \frac{k_v^2 \cdot \pi}{4 \cdot \tan(\frac{\theta}{2})^2}\alpha = \frac{C_p}{C_s} R_e = \frac{U_{s2}}{2n^2 I_{s2}}, \tag{4f}$$

$$D = 1 - \frac{2}{\pi} \cdot \arctan(\frac{1}{wC_pR_e} \cdot \alpha \cdot \{f_{sN}^2 \cdot [1 + (wC_pR_e + \tan(|\beta|)^2)] - 1\} - [wC_pR_e + \tan(|\beta|)] \cdot [1 + \alpha \cdot (1 + \frac{\tan(|\beta|)}{wC_pR_e})]), \tag{4g}$$

in which, n is the turns ratio of the transformer, k_{21} is defined as the AC voltage transmission coefficient, k_v is the coefficient describing the relationship between the output voltage U_{s2} and the input voltage V_{AB1}, U_{DC} is the DC input voltage of the inverter, D is the duty cycle, the voltage gain is M, θ is the normalized value of the conducting angle of the rectifier, f_{sN} is the normalized value for the switching frequency, f_o is the resonant frequency of the C_s and L_s, f_s is the switching frequency of the insulated-gate bipolar transistors (IGBTs), and β is the phase difference between the fundamental voltage and the fundamental current of the transformer.

According to Eqs. (4a)–(4e), the relationship between the voltage gain M and the switching frequency f_s under different load conditions (according to Eq. (4c), Q is proportional to R_e) is shown in Figure 6 (taking $\alpha = 1$). By adjusting the parameters of the resonant component properly, the appropriate gain M and the switching frequency range can be obtained. Figure 6 provides the basis curve for the selection of the switching frequency f_s under different load conditions.

Based on the characteristics of Figure 6, it can be seen that the adjustment range of f_{sN} is very large when the output changes from a light-load to a full-load. On the other hand, the resonant frequency f_o is fixed with the determined resonant components (C_s and L_s). Hence, according to Eq. (4d) the range of the switching frequency f_s is too large to achieve due to the resonant components; the current limited of the IGBTs and the working frequency of the HV rectifier diode. Nevertheless, the proposed power supply works under this condition since the HV bridge arm should turn on or off to charge or discharge the capacitive load. Therefore, in this paper, both the converter switching frequency and the duty cycle are utilized as actuating variables to cope with the large ranges of the output. Hence, the LCC converter can achieve soft-switching over the entire load range with a small adjustment of the switching frequency.
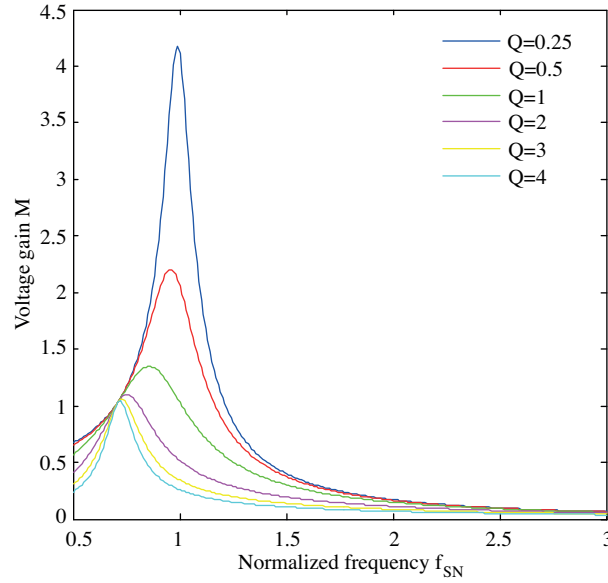
Figure 6. Relationship between the voltage gains M and f_{sN} under different loads.

By adding the small signal disturbance in Eqs. (3a)–(3e), a linear small-signal equation can be obtained after the Laplace transform, and Eqs. (3a)–(3e) can be rewritten as a matrix form.

$$
\begin{pmatrix}
s\Delta i_{Lss}(s) \\
s\Delta i_{Lsc}(s) \\
s\Delta v_{ss}(s) \\
s\Delta v_{sc}(s) \\
s\Delta v_{s2}(s)
\end{pmatrix}
=
\begin{pmatrix}
a11 & a12 & a13 & 0 & a15 \\
a21 & a22 & 0 & a24 & a25 \\
a31 & 0 & 0 & a34 & 0 \\
0 & a42 & a43 & 0 & 0 \\
a51 & a52 & 0 & 0 & a55
\end{pmatrix}
\begin{pmatrix}
\Delta i_{Lss}(s) \\
\Delta i_{Lsc}(s) \\
\Delta v_{ss}(s) \\
\Delta v_{sc}(s) \\
\Delta v_{s2}(s)
\end{pmatrix}
+
\begin{pmatrix}
b11 & b12 \\
b21 & b22 \\
b31 & 0 \\
b41 & 0 \\
b51 & 0
\end{pmatrix}
\begin{pmatrix}
\Delta f_s \\
\Delta d
\end{pmatrix}
\qquad (5)
$$

The coefficients, such as $a11$ and $b11$, are associated with the steady-state operating point, which can be calculated by Appendix A. Different steady-state operating points have different $a11$ and $b11$ coefficients. The transfer function that is essential for the controller design is the transfer function that relates the duty cycle to the output voltage $D_d V_{s2}(s) = \Delta v_{s2}/\Delta d$. According to the value of the actual element in the circuit, we select 5 steady-state operating points to analyze the stability of the controller design. Figure 7a is the frequency response plot of $D_d V_{s2}(s)$ at the 5 steady-state operating points. It can be concluded that in the range of the determined f_s (18 kHz–30 kHz), phase margin and gain margin can meet the rules of stability on all 5 steady-state operating points. Figure 7b shows that the mathematical model predictions match the measurement data well in the range of the actual switching frequency. Therefore, the power supply is stable in the control design.

For the LFP, it is a simple RC series circuit. Therefore, according to Kirchhoff's law, U_{s2} can be described by Eq. (7):

$$
U_{s2} = I_{s2} R_L + U_{s1} = I_{s2} R_L + U_{VLF} \sin(2\pi f_{VLF} t_1), \qquad (6)
$$

where f_{VLF} is the sinusoidal VLF frequency, U_{VLF} is the peak voltage of the VLF output voltage, and t_1 is the time of the sinusoidal VLF.

(a) Bode plot of $DV_{s2}(s)$ for different operating points of the system

(b) Prediction and measurement of $DV_{s2}(s)$ under different
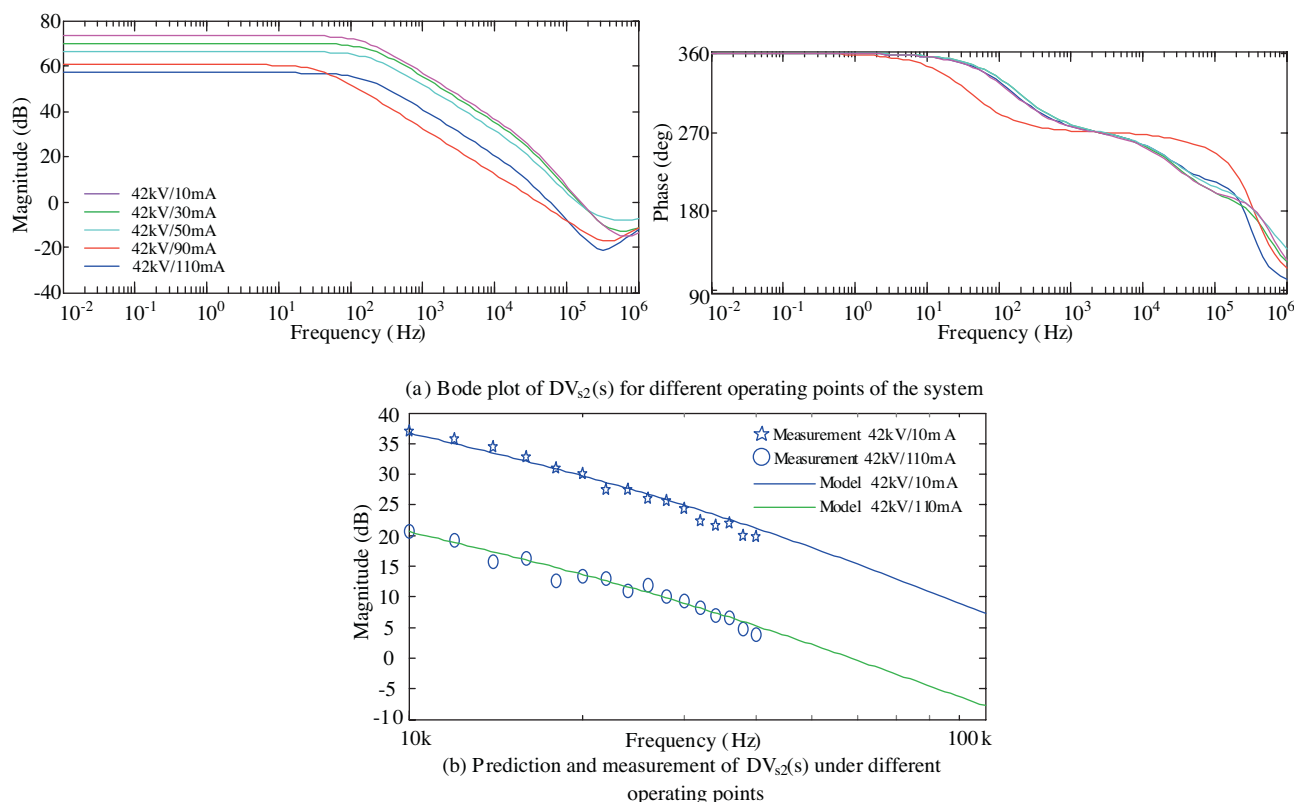operating points

Figure 7. Bode plot of $DV_{s2}(s)$ and the measurement results.

4. Control strategy design

In this paper, both the frequency modulation and the duty cycle modulation control strategy are carried out
to meet the load change in the working conditions. Closed-loop control technology is applied to achieve the
following design purpose.

The purpose of the control unit includes 3 basic aspects:

- Regulate the output voltage U_{s2} at a high frequency.

- Adjust the output voltage U_{s1} at a low frequency.

- Diagnosing the fault to alarm.

Figure 8 shows all of the variables involved in the closed-loop control strategy. The converter presents
the HFP IGBT and the LFP HV bridge arm, the load in Figure 8 presents the HFP (for the HFP it is the
LFP) and the LFP (for the LFP it is R_L and C_L) load, the sampling points are shown in Figure 1. Its input
and output variables are marked by the direction of the arrows. The accuracy of the VLF sinusoidal voltage
is ensured by sampling U_{s1} and the sampling values of U_{s2} and I_{s2} are used to determine the steady-state
operating points and other reference parameters. The type of fault can be diagnosed by U_{s2}, I_{s2}, and I_p.
The specific application of the parameters in Figure 8 is discussed in Figure 9 in detail. Therefore, the control
principles and segmental data processing method of Figure 9 are introduced in the following.
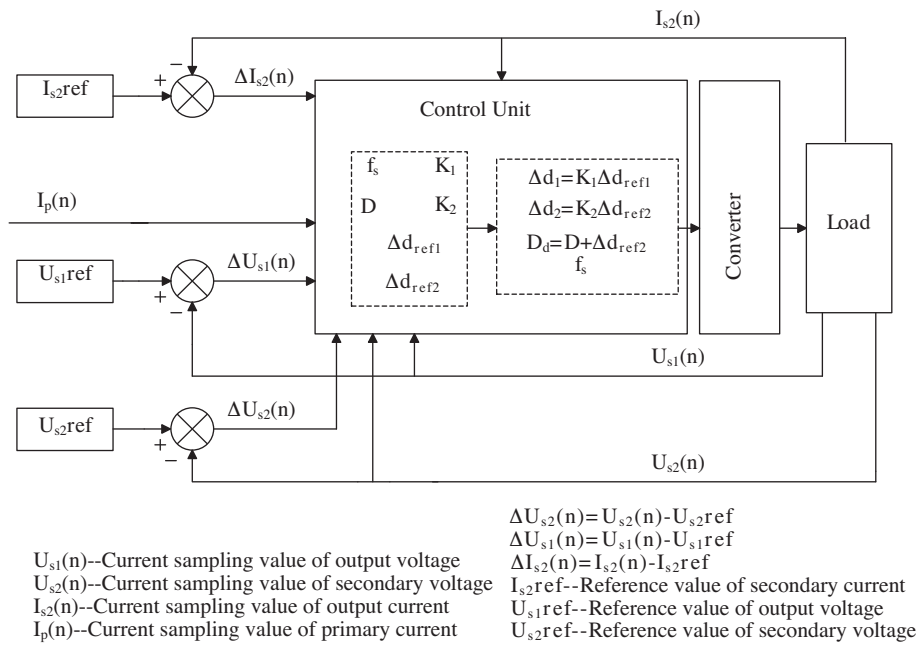
$$\Delta U_{s2}(n)=U_{s2}(n)-U_{s2}ref$$
$$\Delta U_{s1}(n)=U_{s1}(n)-U_{s1}ref$$
$$\Delta I_{s2}(n)=I_{s2}(n)-I_{s2}ref$$

$U_{s1}(n)$--Current sampling value of output voltage
$U_{s2}(n)$--Current sampling value of secondary voltage
$I_{s2}(n)$--Current sampling value of output current
$I_{p}(n)$--Current sampling value of primary current

$I_{s2}ref$--Reference value of secondary current
$U_{s1}ref$--Reference value of output voltage
$U_{s2}ref$--Reference value of secondary voltage

Figure 8. The control strategy of the system.

The rule of small-signal analysis is established in a certain steady-state operating point, which requires a disturbance small. However, the proposed power supply in this paper features in its large load range, if we consider just one working point, when the load changes, the disturbance of the signal will deviate far from the steady-state operating point, losing the rule of the small-signal analysis and may probably lead to the instability of the system. Therefore, it is necessary to select multiple steady-state operating points to cope with different loads. On the other hand, although the control parameters can be obtained through Eqs. (5) and (7), the calculation complexity is too large to be accomplished by the microcontroller unit (MCU). To solve these problems, a special method of data processing named segmental data processing is proposed to decrease the calculation complexity by putting the sample data into segments and lookup tables stored in the ROM, preliminarily to achieve a short response time and precise control. The details of the segmental data processing principle are described in Figure 9. The accuracy of the system is determined by the numbers of the segments in each axis (only the first quadrant is given):

$$\Delta d_{lf} = \frac{U_{s1} - U_{VLF} \sin\left(2\pi f_{VLF} t\right)}{U_{s1} f_{VLF}}, \tag{7}$$

where Δd_{lf} is the variation in duty cycle of the LFP.

In Figure 9a, C_{abc} is one cell of the left graph and the values of $'a'$, $'b'$, $'c'$ are the value in the brackets of $I_{s2}(n)$, $U_{s2}(n)$, $I_{p}(n)$, obtained through the segmental data processing of the sampling value I_{s2} and U_{s2} (e.g., $I_{s2} = 12mA$, $'a' = 1$, $I_{s2} = 26mA$, $'a' = 2$). Once the values of $'a'$, $'b'$, $'c'$ are obtained, the parameters of the steady-state operating point f_s and D can be obtained. $\Delta d_2 ref$ is the optimized parameter after the PI compensator, which represents the reference value of the unit voltage change at a certain steady-state operating point. The overall adjustment of the duty cycle D_d is determined by $D_d = D + K_1 \Delta d_2 ref$. Combined with the sampling value I_p, U_{s2}, and I_{s2}, the type of fault can be diagnosed (e.g., if the value of the unit is C_{115}, we can assert that the fault occurred before the sampling point of U_{s2} and I_{s2}). In most cases, the fault is

(a) Relationship of $I_{s2}(n)$, $U_{s2}(n)$, $I_p(n)$

(b) Relationship of $\Delta I_{s2}(n)$, $\Delta U_{s1}(n)$, $\Delta U_{s2}(n)$
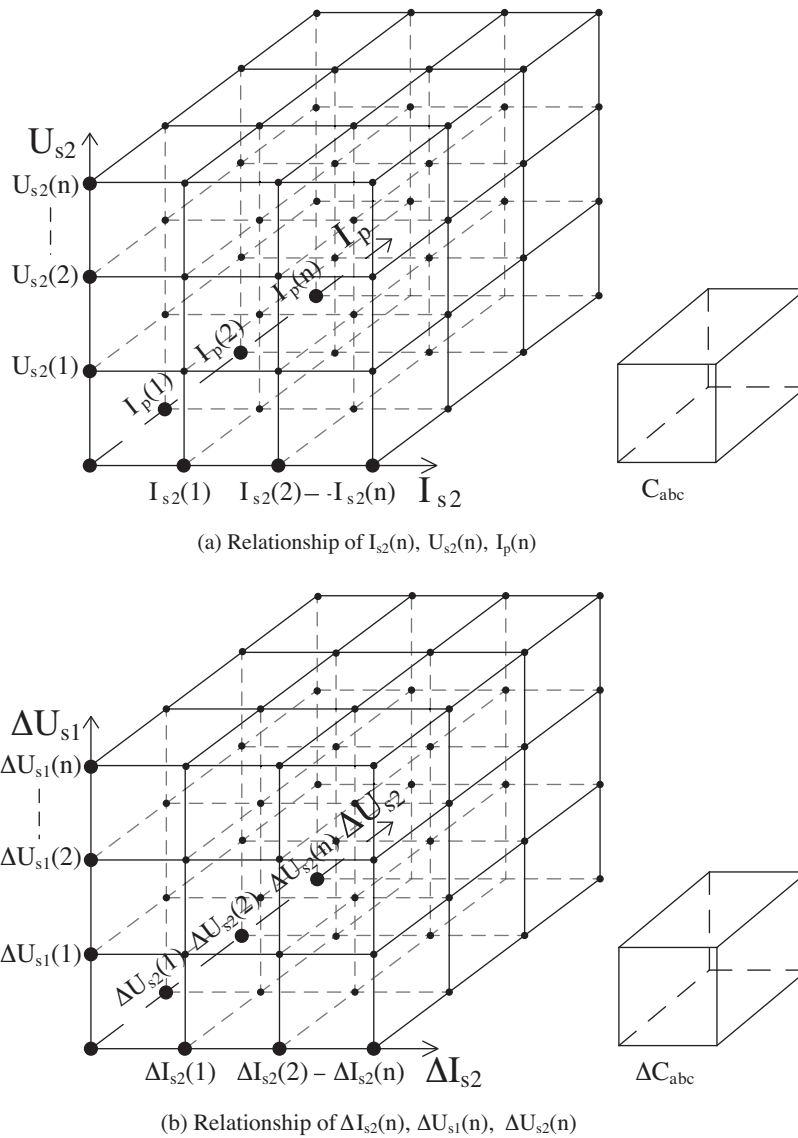
Figure 9. Principle of the segmental-data-processing theory and control strategy.

produced by the transformer breakdown. The type of the fault can be represented by a hexadecimal number error. Hence, 1 C_{abc} unit contains 4 parameters: f_s, D, $\Delta d_2 ref$, and error. All of the C_{abc} in this system are arranged orderly into a table, the MCU obtains these parameters by looking them up in the table after each sampling process, and thus the calculation of the MCU is reduced, thereby enhancing the response speed of the system. The value of ΔU_{s2}, ΔU_{s1}, ΔI_{s2} in Figure 9b is the difference from the U_{s2}, U_{s1}, I_{s1} in Figure 8, and the reference value $U_{s1}ref$, $U_{s2}ref$, $I_{s2}ref$, ΔU_{s2} is related to K_2 in Figure 8. K_2 is the proportional coefficient for Δd_{ref2}, ΔU_{s1} in relation to K_1, K_1 is the proportional coefficient for Δd_{ref1}, and ΔI_{s2} is a criterion when faults occur. Again, a hexadecimal number Δ error can be obtained combined with ΔU_{s1} and ΔU_{s2}, and the value of $'a'$, $'b'$, $'c'$ in ΔC_{abc} can be obtained through the exact method as in Figure 9a; however, the parameters here are different from C_{abc}; they are K_1, K_2, $\Delta d_1 ref$, and Δ error, and Δd_{ref1} is the reference value determined by the standard sine wave through sampling running time. Similarly, ΔC_{abc} are arranged orderly into a table and the MCU obtains these parameters by looking them up in the table.

5. Experimental results

To verify the topology and the control strategy, a 35 kV/0.1 Hz VLF HV generator is designed in the laboratory. The range of input voltage is 180 V–250 V, the boost voltage U_{DC} is 400 V, C_o is 2 μF, C_L is 1.5 μF, and the ratio of the HFHV transformer is 1:100. According to Figure 6 and considering the dead time, the HFP operating frequency f_s varies from 18 kH to 30 kHz; the duty cycle D varies from 0.4 to 0.85, correspondingly; and the operating frequency of the LFP is 1 kHz. The leakage inductance referred to on the primary side of the transformer is 145.4 μH, while the distributed capacitance is 182 nF. While assuming the starting value of $Q = 3$, $\alpha = 1$ under full load conditions, the total series resonant inductor and resonant capacitor are, respectively, 187 μH and 218 nF. Considering the distributed parameter of the transformer, the leakage inductor and distributed capacitance can be used as L_s and C_p ,respectively.

Table is the design steady-state operating point under different I_{s2}. f_s and the range of the T_{on} are determined by I_{s2} (note that if U_{s2} was required to change, f_s and the range of the T_{on} are determined by the combination of I_{s2} and U_{s2}, as illustrated in Figure 9a). When U_{s1} is –42 kV, I_{s2} reaches its maximum and the operating frequency is set to 18 kHz. When U_{s1} is at the peak value of 35 kV, I_{s2} reaches its minimum and the operating frequency is set to 30 kHz. T_{on} changes with the voltage fluctuation of U_{s2}.

Table. Design parameters of the steady-state operating point.

I_{s2}/mA	f_s/kHz	T_{on}/μs
0–20	30.0	3–8
20–40	28.0	8–13
40–60	26.0	12–16
60–70	24.0	15–17
70–100	22.0	16–19
100–120	20.0	19–22
120–150	18.0	21–25

Figures 10a and 10b show the waveform of i_{Ls} under different I_{s2}. When the load changes from a full-load to a light-load, the voltage across the series resonant capacitor U_{Cs} and the current flowing through the series resonant inductor i_{Ls} are also shown in Figures 10a and 10b. It is concluded that at a full-load, the switching frequency f_s is 18 kHz, while the duty cycle D reaches its maximum 0.85 to ensure soft-switching. When there is a light-load, the switching frequency f_s is up to 30 kHz, while the duty cycle D reaches its minimum of 0.4. The series resonant inductor current i_{Ls} and resonant capacitor voltage U_{cp} are sinusoidal over the entire load range. However, the inductor current waveform at a light-load appears intermittent, which is caused by the small duty cycle. At this time, the resonant inductor current leads the voltage across the resonant capacitor; thus, the converter is inductive, but the switch can still achieve a ZCS. Figure 10c is the secondary side HV (U_{sec}) waveform of the HFHV transformer without a rectifier diode. The waveform is close to sinusoidal and it can be concluded that the HV rectifier diode can turn down naturally and that the diode shutdown loss can obviously be reduced. Through the adjustment of the duty cycle and the operating frequency, the IGBTs and antiparallel diodes in the LCC resonant converter achieve soft switching over the entire load range. Figure 10d shows the efficiency of the HFP, where the average efficiency of the DC power supply reaches 87% and the efficiency can reach 75% at a light-load. Therefore, the temperature rise of the transformer is restrained so that the volume of the transformer is reduced.
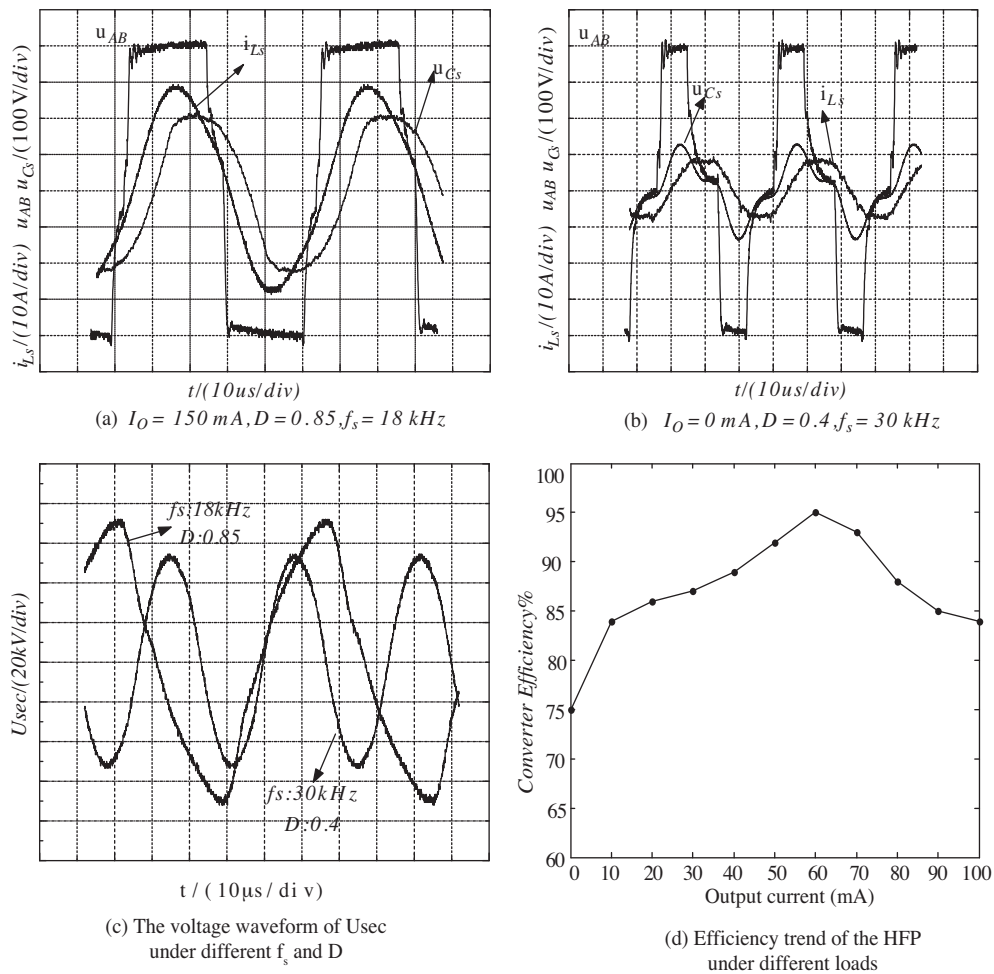
(a) $I_O = 150\, mA, D = 0.85, f_s = 18\, kHz$

(b) $I_O = 0\, mA, D = 0.4, f_s = 30\, kHz$

(c) The voltage waveform of Usec
under different f_s and D

(d) Efficiency trend of the HFP
under different loads

Figure 10. Key waveforms and the efficiency trend of the HFP under closed-loop control.

Figure 11 shows the response time of the step change in the HFP when the output changes from no-load to a full-load. Since the filtering capacitor of the HFP C_o part is just 2 μF, the voltage drop is about 6 kV at the moment of switching. After adopting the closed-loop control strategy and segmentation data processing approach introduced in this paper, it can be seen that the recovery time is 120 μs and there is no instability and overshoot. From the results shown in Figure 11, one can conclude that the control strategy proposed in this paper is correct and stable, and the small-signal mathematical model is correct and effective.

Figure 12 shows the waveforms of U_{s2} and U_{s1} under closed-loop control. Although C_o is just 2 μF, U_{s2} is stable, the ripple of U_{s2} is caused by the step response in Figure 11. The waveform of U_{s1} is sinusoidal and the amplitude of U_{s1} is limited to 35 kV. The control accuracy of the voltage in the system is less than 2% and the THD of U_{s1} is less than 1%, which complies well with the IEEE 400.2 [25], verifying the reliability and stability of the control strategy once again.

The VLF HV generator is shown in Figure 13. The comparison of the traditional power frequency transformer and the HFHV transformer indicates that the volume and weight are reduced distinctly. The weight of the traditional power frequency transformer is 16.5 kg, while the weight of the HFHV transformer is just 2.5 kg. The total weight of the whole VLF HV power supply is less than 20 kg.
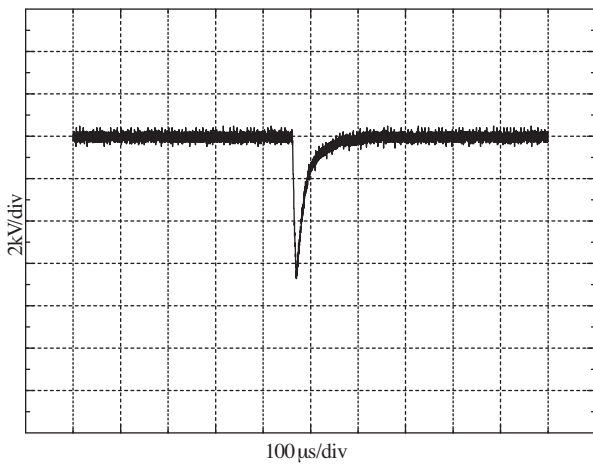
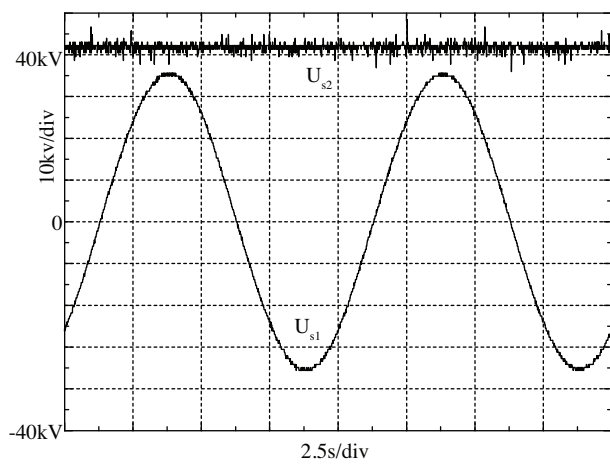**Figure 11.** Response time of the step change from no-load to full-load.

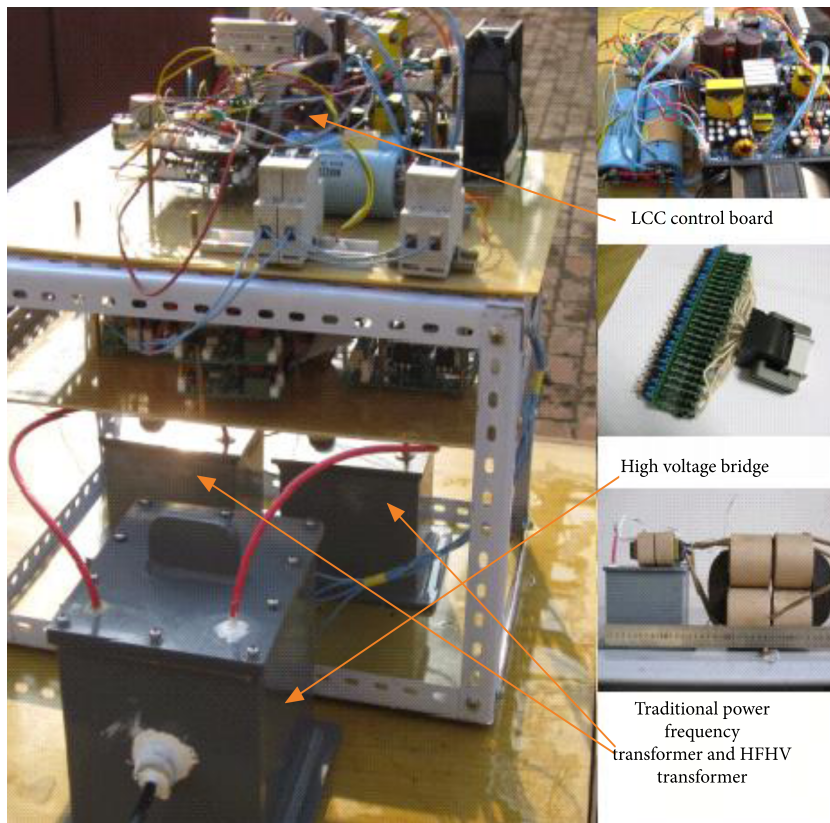**Figure 12.** Output voltage waveform of U_{s2} and U_{s1}.

Figure 13. Photograph of the VLF HV generator and the main parts of the generator.

6. Conclusion

Based on the experiment results the conclusions are drawn as follows:

- The topology of the sinusoidal VLF HV is correct and feasible. Hence, the volume and weight of the generator can be reduced.

- The control strategy is effective and stable. The small-signal mathematical model is correct and effective.

- The test is taken on a 1.5 μF HV capacitor and the THD value is less than 1%, which complies well with the IEEE 400.2.

- By the method of segmental data processing, the calculation complexity obviously is decreased, which ensures that the control strategy can successfully be accomplished in the MCU, taking advantage of the good accuracy of the output voltage and good response time on the step change.

Appendix

$$\theta_{ss} = 2\arctan\sqrt{\frac{\pi}{2C_p\omega_{ss}R_o}} \tag{A.1}$$

$$\alpha_{ss} = \pi - \theta_{ss} + \sin\theta_{ss}\cos\theta_{ss} \tag{A.2}$$

$$\beta_{ss} = \sin^2\theta_{ss} \tag{A.3}$$

$$a_{11} = \frac{4R_o\omega_{ss}C_p\left(1 - \cos\theta\right)\cos\beta_{ss}\cos\alpha_{ss} - \pi\sin^2\theta_{ss}}{\pi^2\omega_{ss}C_pL_s} \tag{A.4}$$

$$a_{12} = \omega_{ss} - \frac{4R_o\omega_{ss}C_p\left(1 - \cos\theta_{ss}\right)\sin\beta_{ss}\cos\alpha_{ss} + \pi\alpha_{ss}}{\pi^2\omega_{ss}C_pL_s} \tag{A.5}$$

$$a_{13} = -\frac{1}{L_s} \tag{A.6}$$

$$a_{15} = \frac{4\cos\beta_{ss}}{\pi L_s} \tag{A.7}$$

$$a_{21} = -\omega_{ss} + \frac{\pi\alpha_{ss} - 4R_o\omega_{ss}C_p\left(1 - \cos\theta_{ss}\right)\sin\delta_{ss}\cos\beta_{ss}}{\pi^2\omega_{ss}C_pL_s} \tag{A.8}$$

$$a_{22} = \frac{4R_o\omega_{ss}C_p\left(1 - \cos\theta\right)\sin\beta_{ss}\sin\alpha_{ss} - \pi\sin^2\theta_{ss}}{\pi^2\omega_{ss}C_pL_s} \tag{A.9}$$

$$a_{25} = \frac{4\sin\beta_{ss}}{\pi L_s} \tag{A.10}$$

$$a_{31} = \frac{1}{C_s} \tag{A.11}$$

$$a_{34} = -\omega_{ss} \tag{A.12}$$

$$a_{42} = \frac{1}{C_s} \tag{A.13}$$

$$a_{43} = \omega_{ss} \tag{A.14}$$

$$a_{51} = \frac{2\cos\beta_{ss}}{\pi C_o} \tag{A.15}$$

$$a_{52} = -\frac{2\sin\beta_{ss}}{\pi C_o} \tag{A.16}$$

$$a_{55} = -\frac{1}{R_o C_o} - \frac{2\omega_{ss} C_p}{\pi C_o} \tag{A.17}$$

$$G_1 = \frac{R_o^2 \left(1 - \cos^2 \theta_{ss}\right)}{4\pi^2 L^s} \tag{A.18}$$

$$G_2 = 2 + \frac{1}{\omega_{ss}^2 C_p L_s} - \frac{\theta_{ss}}{\pi \omega_{ss}^2 C_p L_s} - \frac{2}{\pi \omega_{ss}^2 C_p L_s \tan\left(\frac{\theta_{ss}}{2}\right)} \\ - \frac{R_o^2 \left(1 - \cos^2 \theta_{ss}\right) \tan\left(\frac{\theta_{ss}}{2}\right)}{4\pi^2 L_s} + \frac{R_o(1 - \cos\theta_{ss})}{2\pi^2 \omega_s L_s \tan\left(\frac{\theta_{ss}}{2}\right)} \tag{A.19}$$

$$b_{11} = IL s_{ss} G_1 + IL_{scs} G_2 \tag{A.20}$$

$$b_{21} = IL_{ssc} G_1 - IL_{sss} G_2 \tag{A.21}$$

$$b_{31} = V_{scs} \tag{A.22}$$

$$b_{41} = V_{sss} \tag{A.23}$$

$$b_{51} = \frac{R_o \sqrt{I_{Lsss}^2 + I_{Lscs}^2} \left(1 - \cos\theta_{ss}\right) C_p}{\pi^2 C_o} \tag{A.24}$$

$$b_{12} = \frac{4V_{DC}}{L_s} \cos\left(\frac{d_{ss}}{2}\pi\right) \tag{A.25}$$

$$b_{22} = -\frac{4V_{DC}}{L_s} \sin\left(\frac{d_{ss}}{2}\pi\right) \tag{A.26}$$

$$H_1 = \frac{\omega_{ss} C_p V_{DC}}{\beta_{ss}} \tag{A.27}$$

$$H_2 = \frac{\beta_{ss} C_s}{\alpha_{ss} C_s + \pi C_p - \pi \omega_{ss}^2 L_s C_p C_s} \tag{A.28}$$

$$IL_{sss} = 4H_1 \sin\left(\frac{d_{ss}}{2}\pi\right) - \frac{IL_{scs}}{H_2} \tag{A.29}$$

$$IL_{scs} = \frac{H_1 H_2^2}{(1 + H_2^2)} \left[\frac{4\sin\left(\frac{d_{ss}}{2}\pi\right)}{H_2} + \left[4\cos\left(\frac{d_{ss}}{2}\pi\right) - 1\right] \right] \tag{A.30}$$

$$V_{sss} = \frac{IL_{scs}}{\omega_{ss} C_s} \tag{A.31}$$

$$V_{scs} = \frac{IL_{sss}}{\omega_{ss} C_s} \tag{A.32}$$

References

[1] M.T. Peschel, "Needed changes in medium voltage cable testing. Were you in on it? Welcome to the world of VLF", IEEE International Symposium on Electrical Insulation, pp. 1–5, 2010.

[2] G.S. Eager, B. Fryszczyn, C. Katz, H.A. Elbadaly, A.R. Jean, "Effect of DC testing water tree deteriorated cable and a preliminary evaluation of VLF, as alternate", IEEE Transactions on Power Delivery, Vol. 7, pp. 1582–1589, 1992.

[3] K. Uchida, Y. Kato, M. Nakade, D. Inoue, H. Sakakibara, H. Tanaka, "Estimating the remaining life of water-treed XLPE cable by VLF voltage withstand tests", Furukawa Review 20, pp. 65–70, 2001.

[4] G.S. Eager, C. Katz, B. Fryszczyn, J. Densley, B.S. Bernstein, "High voltage VLF testing of power cables", IEEE Transactions on Power Delivery, Vol. 12, pp. 565–570, 1997.

[5] A. Jaafari, G. Joos, "A compact high voltage low frequency power supply", IEEE Applied Power Electronics Conference and Exposition, Vol. 2, pp. 821–825, 1995.

[6] S. Seesanga, W. Kongnun, A. Sangswang, S. Chotigo, "A new type of the VLF high voltage generator", IEEE 5th International Conference on Electrical Engineering/Electronics, Computer, Telecommunications and Information Technology, Vol. 2, pp. 929–932, 2008.

[7] W. Xinlao, W. Yonghong, C. Qingguo, M. Sen, "A new type of VLF high voltage generator used for on-site tests of power cables", Proceedings of the 5th IEEE International Conference on Properties and Applications of Dielectric Materials, Vol. 2, pp. 113–115, 1997.

[8] W. Kongnun, A. Sangswang, S. Chotigo, "A cascaded H-bridge converter for a new type of the VLF high voltage generator", IEEE 9th International Conference on the Properties and Applications of Dielectric Materials, pp. 89–92, 2009.

[9] R. Reid, "High voltage VLF test equipment with sinusoidal waveform", IEEE Transmission and Distribution Conference, Vol. 1, pp. 8–12, 1999.

[10] Z. Cao, M. Hu, N. Fröhleke, J. Böcker, "Modeling and control design for a very low frequency high-voltage test system", IEEE Transaction on Power Electronics, Vol. 25, pp. 1068–1077, 2010.

[11] L. Yang, P. Fu, X. Liu, "Analysis of the stray capacitances in the transformer of the high-power and high-voltage DC power supply", High Voltage Engineering, Vol. 25, pp. 1403–1408, 2009.

[12] G. Zeng, S. Jin, M. Shi, "Analysis and disposal of distributed capacitance in high frequency and high voltage transformer", Power Electronics, Vol. 26, pp. 54–56, 2002.

[13] J. Liu, L. Sheng, J. Shi, Z. Zhang, X. He, "Design of high voltage, high power and high frequency transformer in LCC resonant converter", IEEE 24th Annual Conference and Exposition on Applied Power Electronics, pp. 1034–1038, 2009.

[14] F.S. Cavalcante, J.W. Kolar, "Design of a 5 kW high output voltage series-parallel resonant DC-DC converter", IEEE 34th Power Electronics Specialist Conference, Vol. 4, pp. 1807–1814, 2003.

[15] A.F. Bakan, "A new LVI assisted PSFB DC-DC converter", Turkish Journal of Electrical Engineering & Computer Sciences, Vol. 19, pp. 191–206, 2011.

[16] G.L. Piazza, R.L. Alves, C. Font, I. Barbi, "Resonant circuit model and design for a high frequency high voltage switched-mode power supply", Brazilian Power Electronics Conference, pp. 326–331, 2009.

[17] L. Lin, H. Zhong, X. Zhang, Y. Zou, "Research on resonant parameters design method of series-parallel resonant capacitor charging power supply", IEEE 6th International Conference on Power Electronics and Motion Control, pp. 561–565, 2009.

[18] G. Çabuk, S. Kılınç, "Reducing electromagnetic interferences in flyback AC-DC converters based on the frequency modulation technique", Turkish Journal of Electrical Engineering & Computer Sciences, Vol. 20, pp. 71–86, 2012.

[19] M. Bruckmann, R. Sommer, M. Fasching, J. Sigg, "Series connection of high voltage IGBT modules", 33rd IEEE IAS Annual Conference on Industry Applications, Vol. 2, pp. 1067–1072, 1998.

[20] A. Consoli, S. Musumeci, G. Oriti, A. Testa, "Active voltage balancement of series connected IGBTs", Conference Record of the 13th IEEE Industry Applications Conference, Vol. 3, pp. 2752–2758, 1995.

[21] I.H. Song, H.S. Ahn, Y.K. Kim, H.S. Shin, C.H. Choi, M.H. Cho, "Development of the 120 kV/70 A high voltage switching system with MOSFETs operated by simple gate control unit", IEEE 33rd Annual Conference on Power Electronics Specialists, Vol. 3, pp. 1181–1185, 2002.

[22] B. Zhang, M.H. Pong, "Dynamic model and small signal analysis based on the extended describing function and Fourier series of a novel AM ZVS direct coupling DC/DC converter", 28th Annual IEEE Conference on Power Electronics Specialists, Vol. 1, pp. 447–452, 1997.

[23] E.X. Yang, F.C. Lee, M.M. Jovanvic, "Small-signal modeling of LCC resonant converter", IEEE 23rd Annual Conference on Power Electronics Specialists, Vol. 2, pp. 941–948, 1992.

[24] M. Hu, N. Frohleke, J. Böcker, "Small-signal model and control design of LCC resonant converter with a capacitive load applied in very low frequency high voltage test system", IEEE Energy Conversion Congress and Exposition, pp. 2972–2979, 2009.

[25] IEEE Guide for Field Testing of Shielded Power Cable Systems Using Very Low Frequency (VLF), IEEE Std 400.2TM-2004, 2004.